

Mapping cell cortex rheology to tissue rheology, and vice-versa

Étienne Moisson^{1,2}, Pierre Seez^{1,2}, Camille Noûs², François Molino^{3,2}, Philippe Marcq^{4,2}, Cyprien Gay^{1,2,*}

1 Laboratoire Matière et Systèmes Complexes, UMR 7057, CNRS and Université Paris Cité, 75205 Paris cedex 13, France

2 Laboratoire Cogitamus, Paris, France

3 Laboratoire Charles Coulomb, UMR 5221, CNRS and Université de Montpellier, Place Eugène Bataillon, F-34095 Montpellier, France

4 PMMH, CNRS, ESPCI Paris, PSL University, Sorbonne Université, Université Paris Cité, F-75005 Paris, France

* Author for correspondence: cyprien.gay@univ-paris-diderot.fr

Abstract

The mechanics of biological tissues mainly proceeds from the cell cortex rheology. A direct, explicit link between cortex rheology and tissue rheology remains lacking, yet would be instrumental in understanding how modulations of cortical mechanics may impact tissue mechanical behaviour. Using an ordered geometry built on 3D hexagonal, incompressible cells, we build a mapping relating the cortical rheology to the monolayer tissue rheology. Our approach shows that the tissue low frequency elastic modulus is proportional to the rest tension of the cortex, as expected from the physics of liquid foams as well as of tensegrity structures. A fractional visco-contractile cortex rheology is predicted to yield a high-frequency fractional visco-elastic monolayer rheology, where such a fractional behaviour has been recently observed experimentally at each scale separately. In particular cases, the mapping may be inverted, allowing to derive from a given tissue rheology the underlying cortex rheology. Interestingly, applying the same approach to a 2D hexagonal tiling fails, which suggests that the 2D character of planar cell cortex-based models may be unsuitable to account for realistic monolayer rheologies. We provide quantitative predictions, amenable to experimental tests through standard perturbation assays of cortex constituents, and hope to foster new, challenging mechanical experiments on cell monolayers.

1. Introduction

The mechanical determinants of embryonic development have received considerable attention in recent years [1, 2, 3], with an emphasis on ingredients such as surface tension, fluid flows, active stresses or boundary conditions. Of note, the complex rheology of tissues [4] harbours immediate consequences for morphogenetic processes [5], as the response of cells to forces within the tissue depends on, *e.g.*, whether the tissue rheology is elastic rather than viscous on the relevant time scale.

Since *in vivo* measurements remain arduous, rheologists have naturally turned to *in vitro* tissues such as epithelial cell aggregates and monolayers, for relative ease of use and control. In the case of cellular aggregates, a variety of techniques has been brought to bear, among which micropipette aspiration [6], parallel plate compression [7] or magnetic rheometry [8], unraveling a complex rheological behaviour that can be viewed as combinations of elastic, viscous, plastic and fractional elements. Epithelial cell monolayers cultured on a flat substrate have revealed an active [9, 10] and viscoelastic [11] rheology on a time scale longer than one hour. In the absence of a substrate, suspended epithelial monolayers held by adhesive micromanipulators [12, 13] have been characterized by a composite fractional model [14] on a time scale shorter than a few minutes.

Tissues being assemblies of mechanically coupled cells, one generally expects tissue rheology to depend on cell rheology [4]. In turn, cell rheology is highly dependent on cytoskeletal rheology [15], both known since early micro-rheological measurements [16, 17] [18, 19] to display a power-law behaviour. The cell cortex, principally made of actin, myosin, and their cross-linkers [20], is generally thought to behave as a viscoelastic material, liquid at time scales large compared to the turnover times of its constituents [21]. Frequency-dependent measurements in single cells submitted to uniaxial compression have confirmed that the cell cortex behaves as a viscoelastic liquid [22]. Similar experiments have shown that the cell cortex Poisson ratio ranges typically from 0.2 to 0.6, decreasing with frequency [23]. Within tissues, cellular cortices in contact form cell-cell junctions. Using optical tweezers, the viscoelastic time of a cell junction has been measured in the *Drosophila melanogaster* embryo, and is of the order of one minute [24]. More recently, the out-of-plane rheology of the cell-cell junction in a cell doublet has been studied experimentally thanks to the introduction of novel micromanipulation techniques [25]. The mechanical response of apical cortices has been probed by atomic force microscopy in epithelial cell monolayers [26], and by laser ablation in *Caenorhabditis elegans* and zebrafish [27].

Because most perturbations of tissue mechanical behavior operate in practice at the sub-cellular level, it is essential (and it remains a challenge) to relate the mechanical properties and descriptions at the microscopic (cell) and macroscopic (tissue) levels. The elastic properties of inert cellular materials can be computed as a function of cell elasticity [28] in the case of solid walls or as a function of cell surface tensions in the case of liquid foams [29, 30]. The study of living cellular materials remains less advanced, although, *e.g.*, the mechanics of lungs has been investigated in the framework of hexagonal networks of elastic springs [31, 32, 33]. A popular cell-based computational model of a cell monolayer is the cell vertex model [34, 35]. This model is based on an energy function, together with a viscous friction on the substrate, which eases computation. The latter is an external force. Hence, in this model the monolayer by itself is conservative and the corresponding effective macroscopic rheology is purely elastic. The corresponding elastic moduli are expected to scale like the rest tension of the cell cortex divided by the cell size, by analogy with a classical result for liquid foams [36, 37]. The tissue-scale elastic stress based on the 2D vertex model has been computed considering in-plane [38] and out-of-plane deformations [39]. To the best of our knowledge, the case of the 3D vertex model [40] has not been addressed from this perspective. When

topological transitions such as cell intercalations (also called cell rearrangements) are allowed, the rheological behavior of a 2D vertex model becomes fluid [41], as anticipated from a theoretical viewpoint [42] (see also [38, 43] for predictions of nonlinear rheological behaviour when topological transitions are included). Tissue behaviours such as tissue deformations and possibly cell intercalations [44] may then be reproduced using different and/or slowly varying tensions among the various cell-cell junctions, thus possibly mimicking internal gene expression levels in cells. However, vertex models do not consider non-trivial cortical rheologies such as observed in studies of single cells or single junctions. As argued in [45], models of cell junction mechanics should now include dissipative effects.

In the present work, we take into account the truly complex mechanical behaviour of the cellular cortex and use it in a cell-based model to derive the corresponding rheological behaviour at the scale of the tissue. Defining a regular cell network geometry allows to derive this connection analytically, leading to general expressions mapping the cortex to the tissue rheology. Existing results are discussed in view of these expressions. As we address the in-plane rheology of the cell monolayer, viewed as a 2D material, our results connect naturally to suspended monolayer experiments [12, 13].

As studies focusing on measurements of tissue or cell response to short time stimuli remain infrequent [12, 13, 24, 46], we focus on timescales up to 10 minutes, well below the viscoelastic time of about 1 hour, characteristic of epithelial cell monolayers [11]. Beyond that timescale, the tissue becomes fluid, as a result of such mechanisms as cell rearrangement, cell division and apoptosis [47]. We expect [42] that this fluid response expected at long time scales will combine in series with the solid viscoelastic behaviour established in the present work.

The article is organized as follows. We first describe the (three-dimensional) geometry, the assumed cell properties and the calculation methodology (Section 2). We then present the resulting monolayer viscoelastic properties and compare them with recent measurements (Section 3). The inverse mapping from the monolayer properties to the cell-scale properties is possible in various ways using some additional assumptions (Section 4). We finally conclude and discuss our results (Section 5).

2. Model

Our simple approach relies on several ingredients, summarized on Fig. 1 and detailed in Section 2.1. Notations are defined on Figs. 1-2 and in their captions. The method for deriving the resulting monolayer moduli is then exposed in Section 2.2.

2.1. Ingredients

Geometry

The cell monolayer is assumed to be a regular arrangement of hexagonal cells with constant height Z , see Fig. 1, with lateral facets a and b (often called *cell-cell junctions*), and horizontal facets c (both basal and apical).

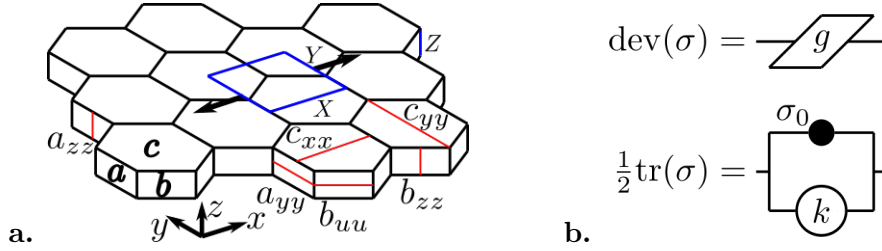


Figure 1.: **Model ingredients:** **a.** Geometry: hexagonal cells tile the plane, with flat facets a , b and c . A representative, rectangular region of the monolayer is drawn in blue, with a volume $V = XYZ$. Relevant facets are labeled a , b (lateral) and c (horizontal). Principal axes of the facets are drawn in red. **b.** Rheological diagrams for the cortex corresponding to Eq. (5) and (6), with the traceless and isotropic components of the stress. Here, as well as in Fig. 3, the (complex) shear modulus g is represented by a parallelogram, the (complex) compression modulus k by a circle, the rest tension σ_0 by a filled disk.

Keeping in mind the boundary conditions imposed onto the suspended monolayer studied in [12, 13, 14], we assume that the monolayer is being stretched or compressed uniformly along the x -axis with no stress applied along the y -axis or along the vertical direction, z . In this model, all cells therefore remain identical at all times. Possible extensions of these boundary conditions are briefly discussed in Section 5.

Intra-cellular material

We consider the intra-cellular material to behave as an inviscid, incompressible fluid, with pressure p^{3D} and constant volume V , expressed in terms of the dimensions of the representative region, depicted on Fig. 1a, as:

$$V = XYZ. \quad (1)$$

Although cell volume is known to fluctuate in MDCK monolayers over a timescale of 10^3 s [48, 49], this effect is neglected over the shorter time scales considered in this work.

Cortex tension

The cell cortex is known to spontaneously develop a tension, which typically stabilizes at some value that depends on the amount of myosin and ATP present and on the network architecture [20]. Based on this fact, we choose to include a fixed, 2D-isotropic tension, denoted σ_0 , in the isotropic part, $\text{tr}(\sigma)$, of the cortical stress (see Fig. 1b). A typical value of cortex tension is $\sigma_0 = 0.3 \text{ mN m}^{-1}$ [21].

Since this tension may differ between horizontal (σ_{0H}) and lateral (σ_{0L}) facets, we introduce the notation

$$\Psi \equiv \frac{\sigma_{0H}}{\sigma_{0L}}. \quad (2)$$

The tension aspect ratio Ψ is known to affect the tissue behaviour and may trigger monolayer folding [50, 51].

Cortex rheology

In this work, we consider the cortex material to be 2D-isotropic. As a consequence, any variation of the in-plane stress in the cortex, σ , around its rest value, σ_0 , in response to an in-plane deformation, ϵ^{facet} , can be modeled, to linear order, by a pair of (frequency dependent) complex moduli [52, 53]. We choose the compression modulus, k [54], and the shear modulus, g [55]. The variation of the in-plane stress tensor σ of the cortex around its rest value is then classically [56, 53] expressed (here in 2D) as:

$$\sigma - \sigma_0 \mathbf{I} = 2g \epsilon^{\text{facet}} + (k - g) \text{tr}(\epsilon^{\text{facet}}) \mathbf{I}, \quad (3)$$

$$= 2g \text{dev}(\epsilon^{\text{facet}}) + k \text{tr}(\epsilon^{\text{facet}}) \mathbf{I}, \quad (4)$$

where \mathbf{I} is the 2D identity tensor and where ϵ^{facet} is decomposed into its isotropic part $\frac{1}{2} \text{tr}(\epsilon^{\text{facet}}) \mathbf{I}$ and its traceless part $\text{dev}(\epsilon^{\text{facet}}) \equiv \epsilon^{\text{facet}} - \frac{1}{2} \text{tr}(\epsilon^{\text{facet}}) \mathbf{I}$. Similarly, the traceless and isotropic parts of σ are given by:

$$\text{dev}(\sigma) = 2g \text{dev}(\epsilon^{\text{facet}}), \quad (5)$$

$$\frac{1}{2} \text{tr}(\sigma) = \sigma_0 + k \text{tr}(\epsilon^{\text{facet}}), \quad (6)$$

which is depicted schematically on Fig. 1b. Let us recall another classical pair of coefficients, namely the Young modulus, e , and the Poisson ratio, ν_c . They are best suited for a situation in which the cortex is being deformed in one of its in-plane directions, while no force is exerted in the other in-plane direction. The Young modulus is then the ratio of the stress to the deformation in the active direction, while the Poisson ratio is the relative amount of induced deformation in the other direction. Note that for most materials, the sign of the latter is the opposite of that of the former, and the Poisson ratio is conventionally positive for a material with such a behaviour. More precisely, the variation of the in-plane stress tensor σ of the cortex around its rest value is expressed in terms of e and ν_c as:

$$\sigma - \sigma_0 \mathbf{I} = \frac{e}{1 + \nu_c} \epsilon^{\text{facet}} + \frac{e \nu_c}{1 - \nu_c^2} \text{tr}(\epsilon^{\text{facet}}) \mathbf{I}, \quad (7)$$

$$= \frac{e}{1 + \nu_c} \text{dev}(\epsilon^{\text{facet}}) + \frac{e}{2(1 - \nu_c)} \text{tr}(\epsilon^{\text{facet}}) \mathbf{I}. \quad (8)$$

They are related to k and g through the following classical expressions, valid in two dimensions [52, 53]:

$$\frac{1}{e} = \frac{1}{4k} + \frac{1}{4g}, \quad (9)$$

$$\nu_c = \frac{k - g}{k + g}. \quad (10)$$

In the incompressible cortex limit ($\nu_c \rightarrow 1$), which is probably rather unrealistic according to the work by Mokbel *et al.* [23], Eqs. (7-8) behave in the classical manner [53]: the denominator in the last term diverges and is compensated by a vanishing isotropic component of the deformation (trace), to accommodate any finite isotropic component of the stress on the left-hand side.

Due to the inner dissipative components of the cortex, it is reasonable to expect that the amplitudes of its moduli increase with frequency (see Appendix B for a discussion of this point). In what follows, in order for the tension σ to remain equal to σ_0 at rest within the framework of Eqs. (5-6), we shall assume more precisely that the amplitudes of cortex shear (g) and compression (k) moduli vanish in the low frequency limit $\omega \rightarrow 0$.

Rest state

As a consequence of the above assumptions, when the monolayer is left at rest, *i.e.*, with no applied in-plane stress, hexagons are fully symmetric, and elementary force balance considerations lead to the following relations between the cell pressure (p_0^{3D}), the dimensions of the representative volume (X_0 , Y_0 and $Z = Z_0$), the tension aspect ratio Ψ , and the cell volume ($V = V_0$) at rest:

$$X_0 = \sqrt{3} \ell_0, \quad (11)$$

$$Y_0 = \frac{3}{2} \ell_0, \quad (12)$$

$$\frac{Z_0}{X_0} = \Psi, \quad (13)$$

$$V = \frac{3\sqrt{3}}{2} \ell_0^2 Z_0 = \frac{9\Psi}{2} \ell_0^3, \quad (14)$$

$$p_0^{3D} = \frac{4\sigma_{0L}}{\sqrt{3}\ell_0} = \frac{4\sigma_{0H}}{3Z_0}, \quad (15)$$

where ℓ_0 is the rest value of both ℓ_a and ℓ_b (see Fig. 2).

Importantly, Eq. (13) shows that the rest tension ratio Ψ coincides with the cell aspect ratio Z_0/X_0 at rest. Larger values of Ψ thus correspond to a columnar epithelium, smaller values to a squamous epithelium, while the monolayer will be made of cuboidal cells when $\Psi \sim 1$.

2.2. Model resolution

The linear response is isotropic

In the present work, the monolayer is viewed as a two-dimensional object in the xy -plane, with in-plane stress components integrated over its thickness Z . With the present choice of cortex 2D isotropy and cytoplasm 2D (and even 3D) isotropy, the only possible source of monolayer 2D anisotropy could lie in the spatial arrangement of cells: here, the regular honeycomb geometry warrants the 2D isotropy of the monolayer linear mechanical response (see [57, 28, 58] for a derivation in the case of an elastic solid).

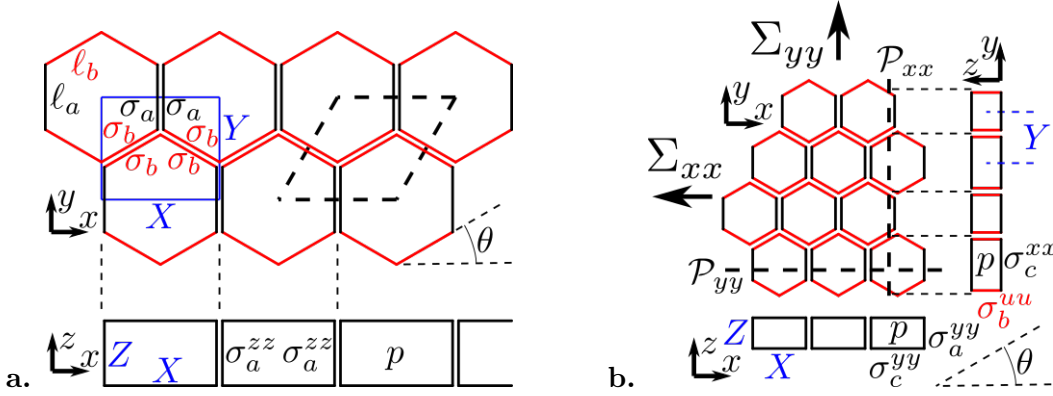


Figure 2.: **Views of the monolayer, force balance and macroscopic stress.**

a. Top: top view. The facet lengths ℓ_a and ℓ_b and the orientation θ of b facets, are shown. The repeating unit is shown as a dashed parallelogram. A simpler representative rectangular region, of same surface area XY , is shown in blue as in Fig. 1. Force balance between three neighbouring cells: at the meeting point within the blue rectangle, all six cortex tensions add up vectorially to zero, which yields Eq. (16) (notations σ_a^{yy} and σ_b^{uu} have been simplified for clarity). **Bottom:** vertical cross-section along in the xz -plane. The force balance in the vertical direction implies that the pressure p in the cytoplasm integrated over the whole cell width X balances the tensions σ_a^{zz} on either side of the cell, as expressed by Eq. (17).

b. Macroscopic stress. The yy component of the in-plane macroscopic stress, Σ_{yy} , can be expressed by counting all forces that are exerted across a perpendicular plane \mathcal{P}_{yy} , represented as a dashed horizontal line. Such forces are readily enumerated from the monolayer cross-section in the xz plane shown below the top view. They include the pressure p in the cell (integrated over the monolayer thickness, Z), the tension σ_c^{yy} of both horizontal layers, as well as the tensions σ_a^{yy} of the relevant lateral facets, integrated over the facet height Z . This provides the expression of Eq. (30). The expression of the xx component Σ_{xx} , provided by Eq. (29), is obtained in a similar way (see monolayer cross-section in the yz plane on the right-hand side), except that the lateral facet tensions, σ_b^{uu} , must be projected onto the x axis (angle θ , see also Fig. 1).

Force balances

Velocities and accelerations in such monolayers are so small that inertial contributions to force balances are negligible (a situation similar to low Reynolds number regimes in fluids). As for in-plane forces, the balance between all six cortex tensions that are exerted on a given vertical edge, such as the vertex at the center of the blue rectangle in the top-view of Fig. 1a or 2a, can be expressed as:

$$2\sigma_a^{yy} \sin(\theta_a) - 4\sigma_b^{uu} \sin(\theta_b) = 0, \quad (16)$$

where σ_a^{yy} and σ_b^{uu} are the horizontal components of the tensions in facets a and b , see Fig. 2 for details.

In the present, simplified geometry, all cells play the same role and all adjacent cells have equal pressures. Lateral cortices, being under tension, are correspondingly flat. Because the monolayer is assumed to be subjected to zero external forces in the z -direction, the force balance at mid-height implies that the pressure p^{3D} in the cell is compensated by the z -tension in the lateral facets at all times (in-plane surface area XY , horizontal lengths ℓ_a and ℓ_b):

$$p^{3D} XY = 2 \sigma_a^{zz} \ell_a + 4 \sigma_b^{zz} \ell_b. \quad (17)$$

In the context of the cross-section depicted in the bottom of Fig. 2a, this simply reads: $p^{3D} X = 2 \sigma_a^{zz}$.

For the sake of simplicity, we here consider that horizontal (apical and basal) facets remain flat despite the larger pressure in the cell as compared to the outside medium, as if these facets were not flexible.

Deformation of the rectangular representative volume

As mentioned in Section 2.1, the monolayer is being stretched along the x -axis, with no forces applied along the perpendicular directions. As a result, the distances $X = 2 \ell_b \cos \theta$ and $Y = \ell_a + \ell_b \sin \theta$ depicted on Fig. 2a (with initial values X_0 and Y_0 , respectively) are related to the monolayer deformation components along the x - and y -axes through:

$$\epsilon_x = \frac{X - X_0}{X_0}, \quad (18)$$

$$\epsilon_y = \frac{Y - Y_0}{Y_0}. \quad (19)$$

In our calculation, we assume that the horizontal facets (index c) deform homogeneously and affinely, that is, in the same proportions as the monolayer, although that is not strictly true (see Appendix D for detail). As a result, the in-plane stress in the horizontal facets can be expressed from Eqs. (5-6) and Eqs. (18-19) in terms of their compression (k_H) and shear (g_H) moduli as:

$$\sigma_c^{xx} = \sigma_{0H} + k_H (\epsilon_x + \epsilon_y) + g_H (\epsilon_x - \epsilon_y), \quad (20)$$

$$\sigma_c^{yy} = \sigma_{0H} + k_H (\epsilon_x + \epsilon_y) + g_H (\epsilon_y - \epsilon_x). \quad (21)$$

For the lateral facets (indices a and b), we similarly define:

$$\epsilon_a = \frac{\ell_a - \ell_0}{\ell_0}, \quad (22)$$

$$\epsilon_b = \frac{\ell_b - \ell_0}{\ell_0}, \quad (23)$$

$$\epsilon_z = \frac{Z - Z_0}{Z_0}. \quad (24)$$

Again, using Eqs. (5-6) and Eqs. (22,23,24), we express the in-plane stress components of the lateral facets in terms of their compression (k_L) and shear (g_L) moduli as:

$$\sigma_a^{yy} = \sigma_{0L} + k_L (\epsilon_a + \epsilon_z) + g_L (\epsilon_a - \epsilon_z), \quad (25)$$

$$\sigma_a^{zz} = \sigma_{0L} + k_L (\epsilon_z + \epsilon_a) + g_L (\epsilon_z - \epsilon_a), \quad (26)$$

$$\sigma_b^{uu} = \sigma_{0L} + k_L (\epsilon_b + \epsilon_z) + g_L (\epsilon_b - \epsilon_z), \quad (27)$$

$$\sigma_b^{zz} = \sigma_{0L} + k_L (\epsilon_z + \epsilon_b) + g_L (\epsilon_z - \epsilon_b). \quad (28)$$

Expression of monolayer in-plane stress

The hexagonal symmetry of the monolayer and our choice to exert forces along the x -axis ensure that the macroscopic stress Σ has principal components along axes x and y . The stress along the x -axis is readily expressed by considering all forces that cut a section perpendicular to the x -axis, as illustrated on Fig. 2b:

$$\Sigma_{xx} = 2\sigma_c^{xx} - p^{3D} Z + \frac{4\ell_b Z}{XY} \sigma_b^{uu} \cos^2 \theta. \quad (29)$$

Similarly for the stress along the y -axis:

$$\Sigma_{yy} = 2\sigma_c^{yy} - p^{3D} Z + \frac{2\ell_a Z}{XY} \sigma_a^{yy} + \frac{4\ell_b Z}{XY} \sigma_b^{uu} \sin^2 \theta. \quad (30)$$

Monolayer in-plane complex moduli

Combining Eqs. (1-28) and imposing that Σ_{yy} remains equal to zero when the monolayer is deformed in the x -direction, we derive as a function of ϵ_x the expressions of the in-plane stress Σ_{xx} in the x -direction and of the deformation ϵ_y in the y -direction. From these two quantities Σ_{xx} and ϵ_y , we derive the complex Young modulus E and the complex Poisson ratio N of the monolayer, viewed as a two-dimensional material:

$$E = \frac{\Sigma_{xx}}{\epsilon_x}, \quad (31)$$

$$N = -\frac{\epsilon_y}{\epsilon_x}. \quad (32)$$

By combining the Poisson ratio and the Young modulus, we may then derive any other complex modulus, for instance the in-plane compression and shear moduli of the monolayer:

$$K = \frac{E}{2(1-N)}, \quad (33)$$

$$G = \frac{E}{2(1+N)}. \quad (34)$$

3. Mapping cortex (micro-)rheology to tissue (macro-)rheology

3.1. General result

In practice, the calculations outlined in Section 2.2 were performed with GNU-Maxima, see Appendix A.

We now express the 2D tissue moduli as obtained following the path outlined above.

For the sake of clarity, we express E and N in terms of K and G which have simpler expressions:

$$K = 3\sigma_{0H} + 2k_H + \Psi k_L + 9\Psi g_L, \quad (35)$$

$$G = \sigma_{0H} + 2g_H + \frac{1}{\frac{1}{2\sigma_{0H}} + \frac{1}{2\Psi k_L + 2\Psi g_L}}, \quad (36)$$

$$\frac{1}{E} = \frac{1}{4K} + \frac{1}{4G}, \quad (37)$$

$$N = \frac{K - G}{K + G}. \quad (38)$$

where indices H and L for rest tensions (σ_0), compression (k) and shear (g) moduli refer to horizontal and lateral facets, respectively, see Eqs. (2), (20, 21) and (25-28) for reference. Expressions (35-37) can be represented conveniently as rheological diagrams, see Fig. 3. They map cortex (micro-) rheology to tissue (macro-) rheology. In the absence of tissue prestress as assumed for the rest state characterized by Eqs. (11-15), the 3D moduli K , G and E may be obtained from the above 2D moduli by dividing by the monolayer thickness.

The monolayer compression modulus K depends obviously on the compression modulus k_H of the horizontal (in-plane) facets. Somewhat surprisingly, it also depends on the shear modulus of lateral facets, g_L . That reflects the fact that elongating the monolayer in an isotropic manner causes cells to flatten, hence lateral facets are elongated horizontally and shrink vertically, see Fig. 6 in Appendix D. In fact, even the lateral facet *surface area* is then required to change due to the constant volume assumption, expressed by Eq. (14). That explains that the monolayer compression modulus K also depends on the lateral facet compression modulus k_L . As a result, in the limit of incompressible horizontal or lateral cortices ($k_H \rightarrow \infty$, $k_L \rightarrow \infty$, which is probably not realistic [23]), the monolayer would become incompressible ($K \rightarrow \infty$, $N \rightarrow 1$).

As stated above (see Eqs. (2,13)), the cell aspect ratio reflects the ratio Ψ of the spontaneous tensions of horizontal and lateral facets. Remarkably, while K is dominated by the moduli of lateral facets for large values of Ψ (columnar cells) and by the moduli of horizontal facets for small values of Ψ (flat cells), by contrast G is dominated by the moduli of horizontal facets for both monolayers made of very columnar and very flat cells ; only for monolayers made of cuboidal cells does G depend substantially on the moduli of lateral facets.

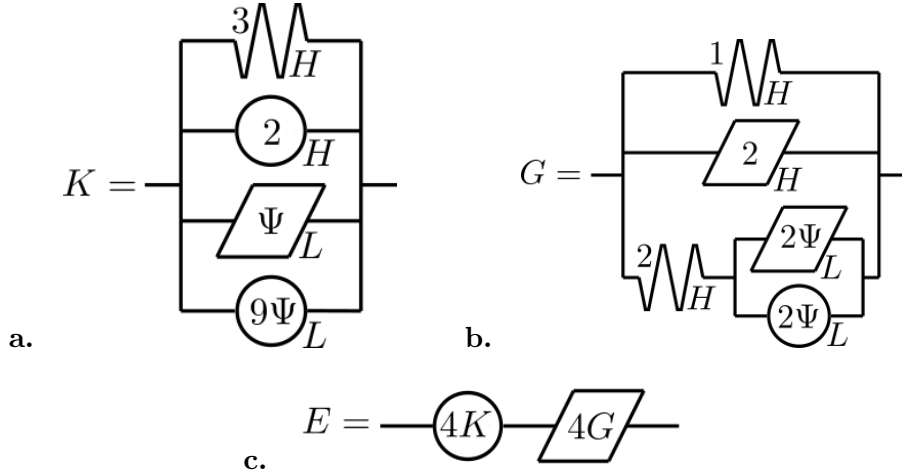


Figure 3.: **Rheological diagrams for the monolayer.** **a.** and **b.** The monolayer compression modulus K and shear modulus G can be viewed as a mechanical arrangement of cortex properties. The symbols are those of Fig. 1. Note that cortical tensions σ_0 in Fig. 1 become springs in the present figure (with identical physical units). The coefficients are those of Eqs. (35) and (36), respectively. Ψ is defined by Eq. (2). Indices H and L refer to horizontal *vs.* lateral facets. **c.** The monolayer Young modulus E can be viewed as equivalent to 4 times its compression modulus K in series with 4 times its shear modulus G .

3.2. Low frequency limit

In the low frequency limit, since g_L , k_L , g_H and k_H tend to zero, tissue moduli are predicted to depend only on the tension of horizontal facets, σ_{0H} , and to be real numbers:

$$K_0 = 3\sigma_{0H}, \quad (39)$$

$$G_0 = \sigma_{0H}, \quad (40)$$

$$E_0 = 3\sigma_{0H}, \quad (41)$$

$$N_0 = 1/2, \quad (42)$$

The monolayer behaves as a purely elastic material in this limit.

In addition, we find that the above in-plane, 2D moduli are proportional to the cortex rest tension σ_{0H} , as expected from the physics of liquid bubble monolayers at time scales where bubbles and films are stable [29, 30]. This is of course expected from dimensional arguments, as both the cortex and the monolayer are two-dimensional and their moduli correspondingly have the same physical units (N/m). Remarkably, however, tissue moduli do not even depend on the cell aspect ratio Ψ , in other words on the horizontal to lateral facet tension ratio.

An additional interpretation of these results is that cell monolayers as well as liquid foams are examples of *tensegrity structures* [59] which contain prestress, even at rest. In

this context, in the case of elastic structures, it has been known for several decades that the linear elastic moduli are proportional to the prestress [60]. In the context of liquid foams or cell monolayers, some elements are under finite compression (bubble gas, cell cytoplasm) while other elements are correspondingly under finite tension (soap films, cell cortices). Note, however, that the origin of the prestress differs. In elastic tensegrity structures, it results from the slight mismatch between each constitutive element individual rest size and its rest size within the structure. In other words, it results from some built-in geometrical frustration. In liquid foams and cell monolayers, by contrast, the constitutive elements under tension (soap films, cell cortices) are fluid, *i.e.*, have no finite individual rest size. The prestress in the structure results from the contractile nature of these particular fluids: surface tension for liquid films, and myosin activity for cell cortices. In other words, liquid foams and cell monolayers are examples of what we may call *contractile fluid tensegrity structures*.

Two aspects of the above prediction (39-42) are testable.

(i). If at least two deformation modes are accessible to assess the monolayer behaviour, then the Poisson ratio can be derived, or equivalently the following ratios can be tested:

$$K_0 = E_0 = 3G_0. \quad (43)$$

(ii). As blebbistatin (or other inhibitors of contractility) lower the rest tension of the acto-myosin cortex [20], then the predicted proportionality of the monolayer elastic moduli to the cell cortex rest tension can be tested by applying such drugs (see, *e.g.*, [9], for a study of the effect of contractility inhibition on epithelial cell monolayer tension).

In physiological conditions, on timescales beyond about 10 minutes, tissues are known to display biological phenomena not considered in the present model, such as cell rearrangements, cell divisions and cell extrusions. Correspondingly, we shall choose 10^{-2} Hz as the lower frequency bound in graphs.

3.3. High frequency limit

In the high frequency limit $\omega \rightarrow \infty$, if the cortex moduli g_L , k_L , g_H and k_H behave elastically, then the monolayer moduli are provided by the full expressions of Eqs. (35-38). However, if they are non-elastic in this limit, hence if their amplitudes go to infinity, we obtain:

$$K_\infty \sim 2k_H + \Psi(k_L + 9g_L), \quad (44)$$

$$G_\infty \sim 2g_H, \quad (45)$$

$$E_\infty \sim \frac{4(2g_H)(2k_H + \Psi(k_L + 9g_L))}{2g_H + 2k_H + \Psi(k_L + 9g_L)}, \quad (46)$$

$$N_\infty \sim \frac{2k_H + \Psi(k_L + 9g_L) - 2g_H}{2k_H + \Psi(k_L + 9g_L) + 2g_H}. \quad (47)$$

As a consequence, the high frequency scaling behaviour of tissue moduli is identical to that of cortex moduli: a viscous cortex will lead to a viscous tissue; a fractional cortex rheology will lead to a fractional tissue rheology with the same exponent (see Fig. 4

for an example). If the cell state is altered in such a way that the cortical fractional exponent is changed, we predict that the same change will display at the tissue scale.

Whereas the low frequency limit of the Poisson ratio is $N_0 = 1/2$, its high frequency limit N_∞ is expected from (47) to depend on specifics of the cortex moduli.

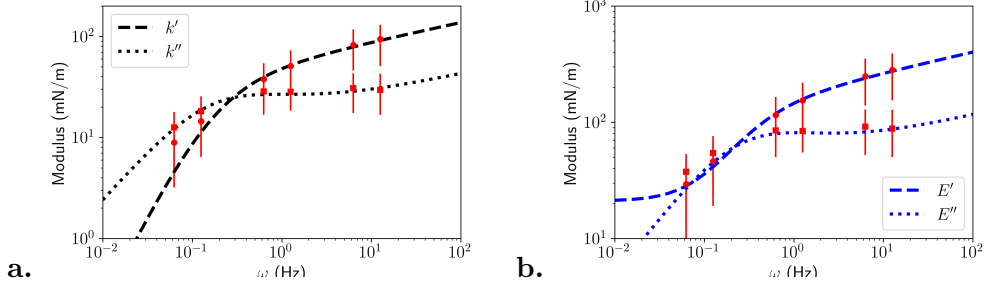


Figure 4.: **Experimental data: cortex rheology.** **a.** Experimental data points from [22] (mN/m), represented by the red symbols and their error bars, are consistent with Eq. (49) (contractile visco-fractional cortex rheology), with the parameter values: $\hat{c} = 60 \text{ mN} \cdot \text{s}^B/\text{m}$, $\hat{\eta} = 250 \text{ mN} \cdot \text{s}/\text{m}$, $\hat{\beta} = 0.19$ (black lines). We observe a low-frequency viscous limit, and a high frequency fractional limit, with exponent B , dominated by the conservation modulus. **b.** Red symbols and their error bars are obtained from data plotted in panel **a** using the mapping (35-38) with $\Psi = 1$, $\sigma_{0H} = \sigma_{0L} = 0.3 \text{ mN m}^{-1}$, $\nu_c = 0.41$ and $g = (1 - \nu_c)k/(1 + \nu_c)$ (blue lines). They are consistent with Eq. (48) (tissue viscoelastic fractional rheology), with the parameter values: $c_\beta = 500 \text{ mN} \cdot \text{s}^B/\text{m}$, $\eta = 170 \text{ mN} \cdot \text{s}/\text{m}$, $\beta = 0.19$, $K_0 = 21 \text{ mN}/\text{m}$. We observe a low-frequency elastic limit, and a high frequency fractional limit, with exponent β , dominated by the conservation modulus. Dashed line: conservation modulus; dotted line: loss modulus.

3.4. Experimental data

Cortex viscoelastic properties have been measured recently as a function of frequency [22, 23] in HeLa cells squeezed between two parallel plates. The more recent work [23] takes precisely into account the spatial variations of the cortex deformation modes during cell compression, with some regions stretched isotropically and other regions subjected to some degree of shear deformation. Assuming that the rheological properties are uniform in the entire cell, it then yields values of the cortex Poisson ratio, found to decrease from 0.66 to 0.17 as frequency increases from 0.1 to 10 Hz, with a mean value $\nu_c \approx 0.41$. This corresponds to the compression modulus, k , being 1.5 to 4 times larger than the shear modulus, g . This work [23], however, does not provide the values and variations of any modulus (shear, compression, etc) separately. In order to map cortex to tissue rheology, we therefore use the cortex complex modulus data points from the older work in the same team [22] (see Fig 4a), although the values thus obtained are a mixture of shear and

compression moduli. More precisely, the compression force is interpreted as if the tension were isotropic and uniform throughout the cortex during compression. As a consequence, the resulting value for the modulus would exactly match the compression modulus in the case of a vanishing shear modulus. For simplicity, we assume it represents the compression modulus when comparing with our results in Section 3.1. We have checked that, by contrast, if it is assumed it represents the shear modulus, our results presented below are unchanged qualitatively, although fitted parameter values are altered.

In Fig 4, we choose a frequency-independent cortex Poisson ratio equal to the average value measured by [23], $\nu_c = 0.41$. We also assume that the cells are cuboidal, $\Psi = 1$. Using a value of all cortex tensions $\sigma_{0H} = \sigma_{0L} = \sigma_0 = 0.3 \text{ mN m}^{-1}$ [21], and assuming that the moduli of lateral and horizontal facets are identical ($k_H = k_L = k$ and $g_H = g_L = g$), the mapping (35-38) yields values of the tissue Young modulus plotted in Fig 4b. As advocated by Bonfanti *et al.* [14], we fitted this data by the following form of the tissue Young's modulus:

$$E^{\text{TVEF}}(\omega) = K_0 + \frac{1}{\frac{1}{i\omega\eta} + \frac{1}{c_\beta(i\omega)^\beta}}, \quad (48)$$

obtaining the parameter values $\eta = (5 \pm 3) 10^2 \text{ mN s m}^{-1}$, $c_\beta = (1.7 \pm 0.7) 10^2 \text{ mN m}^{-1}$, $\beta = 0.185 \pm 0.010$, $K_0 = (2.1 \pm 0.8) 10^1 \text{ mN/m}$. Since HeLa cells are softer and more fluid than MDCK cells, the values of η , c_β and K_0 are at least one order of magnitude lower than obtained for an MDCK monolayer in [14]. Interestingly, the tissue Poisson ratio resulting from our mapping is approximately frequency independent, $N = 0.77 \pm 0.01$.

We next fitted the cortex rheological data plotted in Fig 4a with a model where a dashpot (viscosity $\hat{\eta}$) is combined in series with a fractional element (parameters \hat{c} , $\hat{\beta}$):

$$k_{\text{cortex}}(\omega) = \frac{1}{\frac{1}{i\omega\hat{\eta}} + \frac{1}{\hat{c}(i\omega)^{\hat{\beta}}}}, \quad (49)$$

obtaining the parameter value estimates $\hat{\eta} = (2.5 \pm 1.6) 10^2 \text{ mN s m}^{-1}$, $\hat{c} = (6.0 \pm 2.5) 10^1 \text{ mN m}^{-1}$, $\hat{\beta} = 0.19 \pm 0.01$. Note that Bonfanti *et al.* [14] performed fits of the same data assuming that this rheological diagram was in addition in parallel with a spring of stiffness \hat{k} , at variance with the fluid behaviour expected at long times for the cell cortex. Interestingly, our results allow to map a cortex rheology consistent with Eq. (49) into a tissue rheology consistent with Eq. (48), and to explain the change of magnitude of the corresponding parameter values, with a tissue both stiffer ($c_\beta \simeq 3\hat{c}$), and more viscous ($\eta \simeq 2\hat{\eta}$), than the cell cortex.

3.5. Examples

3.5.1. Fractional cortex rheology

The monolayer moduli shown in Fig 4b, are mapped (through Eqs. 35-38) from a cortex described by Eq. (49) combined with a rest tension σ_0 . They appear to display an intermediate frequency regime. As in the tissue-scale expression (48) by Bonfanti *et*

al. [14], this regime reflects the viscosity component in the cortex rheology. It can be shown that it is no more discernable whenever the viscosity is high enough, namely:

$$\hat{\eta} \gg \hat{c}^{1/\hat{\beta}} \sigma_0^{1-1/\hat{\beta}}. \quad (50)$$

In the limit of Eq. (50), the cortex model of Eq. (49) can be simplified into a simple fractional rheology, which we now explore.

Let all facet moduli (k_H , k_L , g_H , g_L) have the same dependence on frequency, for instance fractional elements with exponent β :

$$k_H(\omega) = k_{H\beta} (i\omega)^\beta, \quad (51)$$

$$k_L(\omega) = k_{L\beta} (i\omega)^\beta, \quad (52)$$

$$g_H(\omega) = g_{H\beta} (i\omega)^\beta, \quad (53)$$

$$g_L(\omega) = g_{L\beta} (i\omega)^\beta, \quad (54)$$

where the prefactors $k_{H\beta}$, etc, are real numbers. These expressions imply that the cortex Poisson ratios for horizontal and lateral facets, given by Eq. (10), are frequency-independent.

The monolayer moduli K and G , given by Eqs. (35,36), can then be approximated at both low and high frequencies by the respective sums of their asymptotic expressions in both limits:

$$K \simeq 3\sigma_{0H} + K_\beta (i\omega)^\beta, \quad (55)$$

$$G \simeq \sigma_{0H} + 2g_{H\beta} (i\omega)^\beta, \quad (56)$$

where $K_\beta = 2k_{H\beta} + \Psi(k_{L\beta} + 9g_{L\beta})$.

If all cortex moduli are fractional, K and G both evolve from elastic at low frequencies (depending only on the cortex tension at rest, σ_{0H}) to fractional at large frequencies. The crossovers at intermediate frequencies depend on the details of the parameter values. This will in particular be the case for a purely viscous cortex ($\beta = 1$).

3.5.2. Maxwell cortex rheology

Another (this time, elastic) limit of the model (49), with $\beta \rightarrow 0$, leads to a Maxwell model for the cortex, with a viscous/elastic behaviour respectively in the low/high frequency limit. Such a model has been proposed for the cell cortex rheology in [61], and reads

$$e^{\text{Maxwell}} = \frac{1}{\frac{1}{i\omega\eta} + \frac{1}{g}}, \quad (57)$$

(see Fig. 5a). In this case, the high-frequency tissue rheological behaviour is elastic (see Fig. 5b), at variance with the power-law behaviour observed experimentally in this limit [14]. This model, introduced by [61], constitutes an interesting heuristic proposal for the cortex mechanics, which incorporates in the most simple manner the ingredients of

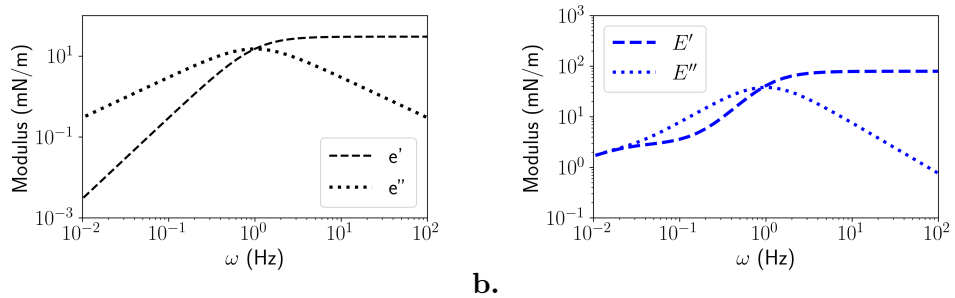


Figure 5.: **Tissue moduli based on a Maxwell cortex rheology.** Dashed lines: conservation moduli; dotted lines: loss moduli (mN/m). **a.** Cortex rheology, Eq. (57), with parameters $\eta = 30 \text{ mN} \cdot \text{s/m}$ and $g = 30 \text{ mN/m}$. **b.** Tissue rheology, obtained using Eqs. (35,36) with parameters $\nu = 0.4$, $\Psi = 1$ and $\sigma_0 = 0.3 \text{ mN/m}$. We obtain a low-frequency (not shown) and a high-frequency elastic limit, with an intermediate dissipative regime.

cortex active tension (σ_0), elasticity (g) due to the actin fiber network, and relaxation (here with a unique timescale η/g) due to monomer and crosslinker stochastic renewal. It has been applied successfully to the microplate single cell experiment [18, 19]. A similar model has been used to account for experimental observations of the effects of single cortex manipulations [62].

4. Inverse mapping of tissue (macro-)rheology to cortex (micro-)rheology

4.1. Low frequency inversion

The low frequency moduli of the monolayer are real numbers according to expressions (39-41). In other words, the monolayer is purely elastic in this limit, with a stiffness proportional to the rest tension of the horizontal cortices, σ_{0H} . This feature allows for a direct access to this cell-scale quantity through macroscopic measurements. The rest tension of the lateral facets, σ_{0L} , is then derived from the cell aspect ratio, Ψ , as a result of Eq. (2):

$$\sigma_{0H} = G_0 = \frac{K_0}{3} = \frac{E_0}{3}, \quad (58)$$

$$\sigma_{0L} = \frac{\sigma_{0H}}{\Psi}. \quad (59)$$

However, the cortical tension of lateral sides σ_{0L} , being absent from both the low and high frequency limits cannot be deduced from such measurements.

In practice, tissues flow over timescales large compared to the typical rearrangement/cell division/cell extrusion times. In [11], the viscoelastic time of a MDCK monolayer on a flat substrate was measured to be of the order of 1 hour. The measurement of the

”low frequency” moduli G_0 , K_0 and E_0 would need to be performed over time scales shorter than this viscoelastic time.

4.2. No general inversion

The most general goal, when attempting to inverse the mapping obtained in Section 3.1, would be the following. Let us assume that sophisticated mechanical measurements provide two independent complex moduli as a function of the angular frequency, for instance: $K(\omega)$ and $G(\omega)$, from which we subtract the low frequency limits:

$$\Delta K(\omega) = K(\omega) - K_0, \quad (60)$$

$$\Delta G(\omega) = G(\omega) - G_0. \quad (61)$$

Once the rest tensions are known from the low frequency analysis, see Eqs. (58,59), the goal is to obtain two independent complex moduli of both the horizontal and the lateral facets: $k_H(\omega)$, $g_H(\omega)$, $k_L(\omega)$ and $g_L(\omega)$.

It is clearly not possible, with no additional assumption, to uniquely determine four such quantities from only both monolayer scale quantities $\Delta K(\omega)$ and $\Delta G(\omega)$. Below, we review some assumption examples and the corresponding expressions of the cortex scale quantities.

4.3. Inversion under tension scaling assumption

In order to go beyond this impossibility, let us now assume that the phenomenon that causes the tension of the horizontal and lateral facets to differ equally applies to the complex moduli. In other words, let us assume that the tension ratio, Ψ , also applies to the moduli, at all frequencies:

$$\frac{\sigma_{0H}}{\sigma_{0L}} = \Psi = \frac{k_H(\omega)}{k_L(\omega)} = \frac{g_H(\omega)}{g_L(\omega)}. \quad (62)$$

If $\Psi = 1$ in addition to this scaling assumption, the rheological properties of all facets would become identical.

With assumption (62), the expressions of K and G , given by Eqs. (35,36) can be rewritten in terms of ΔK and ΔG , see Eqs. (60,61). Using the assumption expressed above as Eq. (62), they can be rewritten in terms of only σ_{0H} , k_H and g_H , with no influence of Ψ :

$$\Delta K = 3k_H + 9g_H, \quad (63)$$

$$\Delta G = 2g_H + \frac{1}{\frac{1}{2\sigma_{0H}} + \frac{1}{2k_H + 2g_H}}. \quad (64)$$

Assuming that not only σ_{0H} , but also ΔK and ΔG are positive real numbers, one can invert these equations and obtain the values of the cortex moduli of the horizontal

facets:

$$k_H = \frac{1}{4} \left(3\sigma_{0H} - \sqrt{D} + \Delta K - 3\Delta G \right), \quad (65)$$

$$g_H = \frac{1}{12} \left(\sqrt{D} - 3\sigma_{0H} + \Delta K + 3\Delta G \right), \quad (66)$$

$$D = 9\sigma_{0H}^2 + 18\sigma_{0H}(\Delta K - 3\Delta G) + (\Delta K - 3\Delta G)^2. \quad (67)$$

The moduli of the lateral facets are then immediately obtained using the cell aspect ratio:

$$k_L = k_H/\Psi, \quad (68)$$

$$g_L = g_H/\Psi. \quad (69)$$

In Eqs. (65,66), the sign in front of \sqrt{D} was chosen so as to satisfy the low frequency limit. The quantities $\Delta K(\omega)$ and $\Delta G(\omega)$ are in fact complex numbers, and one may assume that, as combinations of springs ($\beta = 0$), dashpots ($\beta = 1$) and fractional elements ($0 < \beta < 1$), their real and imaginary parts are both positive. We shall adopt a definition of \sqrt{D} that remains continuous in all accessible regions around the low frequency (real) value $\sqrt{D} = 3\sigma_{0H}$.

Let us consider a first particular situation where the monolayer Poisson ratio N is equal to $1/2$ not only in the low frequency limit but also at all frequencies. Eq. (38) then implies that $K(\omega) = 3G(\omega)$. Hence, we have $\Delta K(\omega) = 3\Delta G(\omega)$. As a consequence, $\sqrt{D} = 3\sigma_{0H}$ is constant. The above results then suggest that, ignoring the influence of their rest tension σ_{0H} , the cortices' bulk moduli vanish, while their shear moduli are directly related to the monolayer shear modulus:

$$\Psi k_L = k_H = 0, \quad (70)$$

$$\Psi g_L = g_H = \frac{1}{2} \Delta G = \frac{1}{2} (G - G_0). \quad (71)$$

In a second particular situation, we assume not only that horizontal and lateral facet moduli are in the same ratio as the rest tension, see Eq. (62), which implies that all facets have identical Poisson's ratio $\nu_c(\omega)$, but we also assume that this value is constant: $\nu_c(\omega) = \text{const}$. It is then more convenient to express the cortex compression and shear moduli, k and g , in terms of the cortex Young modulus e and Poisson ratio ν_c :

$$k_H = \frac{e_H}{2(1 - \nu_c)}, \quad (72)$$

$$g_H = \frac{e_H}{2(1 + \nu_c)}. \quad (73)$$

Eqs. (35,36) then become:

$$K = 3\sigma_{0H} + \frac{6 - 3\nu_c}{1 - \nu_c^2} e_H, \quad (74)$$

$$G = \sigma_{0H} + \frac{1}{1 + \nu_c} e_H + \frac{1}{\frac{1}{2\sigma_{0H}} + \frac{1 - \nu_c^2}{2e_H}}, \quad (75)$$

while the monolayer Young modulus E and Poisson ratio N are then obtained from Eqs. (37, 38). That implies that the cortex moduli can be immediately expressed from the monolayer bulk modulus K :

$$e_H = \frac{1 - \nu_c^2}{6 - 3\nu_c} \Delta K, \quad (76)$$

$$k_H = \frac{1 + \nu_c}{12 - 6\nu_c} \Delta K, \quad (77)$$

$$g_H = \frac{1 - \nu_c}{12 - 6\nu_c} \Delta K. \quad (78)$$

This particular case illustrates how, when $\nu_c(\omega) = \text{const}$, cortex and tissue rheology may be identical, as suggested both by [14] and Fig. 4.

An expression for the monolayer shear modulus G can also be obtained, for instance for the cortex shear modulus g_H :

$$4g_H = \Delta G - (3 - \nu_c)\sigma_{0H} + \sqrt{(\Delta G - (3 - \nu_c)\sigma_{0H})^2 + (1 - \nu_c)\sigma_{0H}\Delta G}. \quad (79)$$

Eqs. (72-73) then readily yield expressions for the Young modulus e_H and compression modulus k_H . Eq. (79) shows that a strong similarity is expected between the frequency dependencies of the (micro-scale) cortex moduli and the (macro-scale) monolayer shear modulus. If in addition, $\nu_c = 1$ (in other words, a possibly unrealistic assumption of a 2d-incompressible cortex), then the tissue becomes incompressible ($K \rightarrow \infty$), Eq. (79) becomes

$$2g_H = \Delta G - 2\sigma_{0H}. \quad (80)$$

If we rather assume $\nu_c = 0$ as in [61], Eqs. (76-78) become $e_H = 2g_H = 2k_H = \Delta K/6$.

5. Discussion and perspectives

To summarize, we characterize in this work the mechanical behaviour of an epithelial tissue by establishing the link between the mechanics at the cytoskeletal scale and the mechanics at the epithelial scale. We describe theoretically the linear rheology of an ordered assembly of hexagonal cells, as a function of those of the cell cortices. We also discuss, in particular cases, the inverse problem that starts from the epithelial rheology and deduces the cortical rheology. In the low-frequency limit, we obtain that the monolayer is elastic, with moduli proportional to the cortex rest tensions, as expected of tensegrity structures. In other frequency ranges, the monolayer rheology reflects the main features of the cortex rheologies.

We hope that this work will be conducive to a better understanding of the contribution of cellular constituents in the epithelial mechanical behaviour. It suggests that the rich rheological behaviour of cell cortices should be taken into account when formulating (disordered) vertex models, beyond the current, standard definition of an energy function based on constant cortex (cell-cell junction) tensions.

In order to test whether the full 3D geometry depicted on Fig. 1a is required to predict the monolayer rheology, we attempted to reduce the dimensionality and considered a regular tiling by *planar* hexagonal cells. As shown in Appendix C, this geometry leads to an elastic high-frequency rheology, at variance with experimental observations. The results of these calculations suggest that, at least for ordered tilings, the rheological behaviour of lateral cell cortices and their mechanical coupling with horizontal cell cortices cannot be ignored when determining the tissue rheology.

Our results are based on several simplifying assumptions that may be relaxed in the future, for instance considering the effect of disorder (whose impact may be assessed by numerical simulations) [63]; an asymmetry in apico-basal tension or moduli [51, 64]; a realistic bulk cell rheology [4] or different boundary conditions [12]. In the experiments [65] a finite initial tension of the monolayer is observed in the x -direction. Moreover, an actin cable is present along each free, lateral edge of the suspended monolayer. These edges being slightly curved, they probably exert some tension on the monolayer in the y -direction. The initial monolayer tension seems isotropic in the xy -plane (see Fig. 2a in [65]). We have here neglected any such initial monolayer tension. While we focused on the planar geometry characteristic of cell monolayers, a natural extension would be to represent a 3D tissue (for instance a cellular spheroid) by a tiling composed of Kelvin cells, for which the low frequency, elastic limit has been established in the field of liquid foams [37].

In this work, the fact that horizontal facets are assumed flat is by itself a simplification. Indeed, force balance implies that a right angle at the edge between lateral and horizontal facets would correspond to horizontal tension values much larger than lateral tension values. A more realistic geometry, with curved apical and basal facets, is left for future studies.

Perhaps more importantly, the cells have more than two in-plane degrees of freedom and they need to obey force balance on vertical edges, see Eq. (16). Hence, even though the rectangular representative volume has to deform exactly in the same proportions as the monolayer, the cells in general do not deform homogeneously, instead they contain some elements that move in a non-affine manner (see Appendix D). Here, however, in order to simplify the description, we calculate the stress in the horizontal facets as if their deformation were homogeneous (and thus identical to the monolayer in-plane deformation).

Implementing and validating the inverse mapping from monolayer to cell cortex rheology, depends practically on the availability of the corresponding experimental measurements. A first valuable contribution would be to test the monolayer in such a way as to measure two independent macroscopic moduli. A second milestone would be to have access to measurements of the cortex rheology of cells within a monolayer rather than of isolated single cells, as pioneered by [24, 25, 26]. That may then help assessing the scaling assumption Eq. (62) put forward in Section 4.3.

We hope that this work will foster more experimental work, measuring both cortex and tissue rheology, in view of the direct and inverse mappings that link them.

6. Acknowledgements

We acknowledge fruitful discussions with Anne Tanguy, Magali Suzanne and Camille Noûs, as well as with Jocelyn Étienne whose cortex rheology model [61] has been a central source of inspiration for the present work. We thank Jonathan Fouchard and François Graner for a careful reading of the manuscript. We also thank the referees for their comments, which helped clarify several aspects.

References

- [1] Carl-Philipp Heisenberg and Yohanns Bellaïche. Forces in tissue morphogenesis and patterning. *Cell*, 153:948–962, 2013.
- [2] Katharine Goodwin and Celeste M. Nelson. Mechanics of development. *Developmental Cell*, 56:240–250, 2022.
- [3] Manon Valet, Eric D. Siggia, and Ali H. Brivanlou. Mechanical regulation of early vertebrate embryogenesis. *Nature Reviews Molecular Cell Biology*, 23:169–184, 2021.
- [4] Claude Verdier, Jocelyn Etienne, Alain Duperray, and Luigi Preziosi. Rheological properties of biological materials. *C.R. Physique*, 10:790–811, 2009.
- [5] Nicoletta I Petridou and Carl-Philipp Heisenberg. Tissue rheology in embryonic organization. *The EMBO Journal*, 38:e102497, 2019.
- [6] Karine Guevorkian, Marie-Josée Colbert, Mélanie Durth, Sylvie Dufour, and Françoise Brochard-Wyart. Aspiration of biological viscoelastic drops. *Phys. Rev. Lett.*, 104:218101, 2010.
- [7] Tomita Vasilica Stirbat, Sham Tlili, Thibault Houver, Jean-Paul Rieu, Catherine Barentin, and Hélène Delanoë-Ayari. Multicellular aggregates: a model system for tissue rheology. *Eur Phys J E Soft Matter*, 36:9898, 2013.
- [8] Gaëtan Mary, François Mazuel, Vincent Nier, Florian Fage, Irène Nagle, Louisiane Devaud, Jean-Claude Bacri, Sophie Asnacios, Atef Asnacios, Cyprien Gay, Philippe Marcq, Claire Wilhelm, and Myriam Reffay. All-in-one rheometry and nonlinear rheology of multicellular aggregates. *Phys. Rev. E*, 2022.
- [9] Romaric Vincent, Elsa Bazellières, Carlos Pérez-González, Marina Uroz, Xavier Serra-Picamal, and Xavier Trepast. Active tensile modulus of an epithelial monolayer. *Phys Rev Lett*, 115:248103, 2015.
- [10] Vincent Nier, Grégoire Peyret, Joseph d’Alessandro, Shuji Ishihara, Benoit Ladoux, and Philippe Marcq. Kalman inversion stress microscopy. *Biophysical Journal*, 115(9):1808–1816, 2018.

- [11] S. Tlili, M. Durande, C. Gay, B. Ladoux, F. Graner, and H. Delanoë-Ayari. Migrating epithelial monolayer flows like a maxwell viscoelastic liquid. *Phys. Rev. Lett.*, 125:088102, 2020.
- [12] Andrew R Harris, Julien Bellis, Nargess Khalilgharibi, Tom Wyatt, Buzz Baum, Alexandre J Kabla, and Guillaume T Charras. Generating suspended cell monolayers for mechanobiological studies. *Nat Protoc*, 8:2516–2530, 2013.
- [13] Nargess Khalilgharibi, Jonathan Fouchard, Nina Asadipour, Ricardo Barrientos, Maria Duda, Alessandra Bonfanti, Amina Yonis, Andrew Harris, Payman Mosaffa, Yasuyuki Fujita, Alexandre Kabla, Yanlan Mao, Buzz Baum, José J Muñoz, Mark Miodownik, and Guillaume Charras. Stress relaxation in epithelial monolayers is controlled by the actomyosin cortex. *Nature Physics*, 15:839–847, 2019.
- [14] A. Bonfanti, J. Fouchard, N. Khalilgharibi, G. Charras, and A. Kabla. A unified rheological model for cells and cellularised materials. *Royal Society Open Science*, 7:190920, 2020.
- [15] Pramod A. Pullarkat, Pablo A. Fernández, and Albrecht Ott. Rheological properties of the eukaryotic cell cytoskeleton. *Phys. Rep.*, 449:29–53, 2007.
- [16] Ben Fabry, Geoffrey N. Maksym, James P. Butler, Michael Glogauer, Daniel Navajas, and Jeffrey J. Fredberg. Scaling the microrheology of living cells. *Phys. Rev. Lett.*, 87:148102, 2001.
- [17] Guillaume Lenormand, Emil Millet, Ben Fabry, James P. Butler, and Jeffrey J. Fredberg. Linearity and time-scale invariance of the creep function in living cells. *Journal of The Royal Society Interface*, 1(1):91–97, nov 2004.
- [18] Nicolas Desprat, Alain Richert, Jacqueline Simeon, and Atef Asnacios. Creep function of a single living cell. *Biophys. J.*, 88:2224–2233, 2005.
- [19] Martial Balland, Nicolas Desprat, Delphine Icard, Sophie Féréol, Atef Asnacios, Julien Browaeys, Sylvie Hénon, and François Gallet. Power laws in microrheology experiments on living cells: Comparative analysis and modeling. *Phys. Rev. E*, 74:021911, 2006.
- [20] Priyamvada Chugh and Ewa K. Paluch. The actin cortex at a glance. *Journal of Cell Science*, 131:jcs186254, 2018.
- [21] Guillaume Salbreux, Guillaume Charras, and Ewa Paluch. Actin cortex mechanics and cellular morphogenesis. *Trends in Cell Biology*, 22:536 – 545, 2012.
- [22] Elisabeth Fischer-Friedrich, Yusuke Toyoda, Cedric J. Cattin, Daniel J. Müller, Anthony A. Hyman, and Frank Jülicher. Rheology of the active cell cortex in mitosis. *Biophysical Journal*, 111:589 – 600, 2016.

- [23] Marcel Mokbel, Kamran Hosseini, Sebastian Aland, and Elisabeth Fischer-Friedrich. The poisson ratio of the cellular actin cortex is frequency dependent. *Biophysical Journal*, 118:1968–1976, 2020.
- [24] Raphaël Clément, Benoît Dehapiot, Claudio Collinet, Thomas Lecuit, and Pierre-François Lenne. Viscoelastic dissipation stabilizes cell shape changes during tissue morphogenesis. *Current Biology*, 27:3132–3142.e4, 2017.
- [25] Amir Monemian Esfahani, Jordan Rosenbohm, Bahareh Tajvidi Safa, Nickolay V. Lavrik, Grayson Minnick, Quan Zhou, Fang Kong, Xiaowei Jin, Eunju Kim, Ying Liu, Yongfeng Lu, Jung Yul Lim, James K. Wahl, Ming Dao, Changjin Huang, and Ruiguo Yang. Characterization of the strain-rate-dependent mechanical response of single cell–cell junctions. *Proceedings of the National Academy of Sciences*, 118:e2019347118, 2021.
- [26] Anna Pietuch, Bastian Rouven Brückner, Tamir Fine, Ingo Mey, and Andreas Janshoff. Elastic properties of cells in the context of confluent cell monolayers: impact of tension and surface area regulation. *Soft Matter*, 9(48):11490, 2013.
- [27] Arnab Saha, Masatoshi Nishikawa, Martin Behrndt, Carl-Philipp Heisenberg, Frank Jülicher, and Stephan W. Grill. Determining physical properties of the cell cortex. *Biophysical Journal*, 110:1421–1429, 2016.
- [28] Lorna J. Gibson and Michael F. Ashby. *Cellular Solids*. Cambridge University Press, 2014.
- [29] D. Weaire and S. Hutzler. *The Physics of Foams*. Oxford University Press, 2001.
- [30] I. Cantat, S. Cohen-Addad, F. Elias, F. Graner, R. Höhler, O. Pitois, F. Rouyer, and A. Saint-Jalmes. *Foams: structure and dynamics*. Oxford University Press, ed. S.J. Cox, 2013.
- [31] J Mead, T Takishima, and D Leith. Stress distribution in lungs: a model of pulmonary elasticity. *Journal of Applied Physiology*, 28(5):596–608, may 1970.
- [32] D. Stamenovic. Micromechanical foundations of pulmonary elasticity. *Physiological Reviews*, 70(4):1117–1134, oct 1990.
- [33] Francisco S. A. Cavalcante, Satoru Ito, Kelly Brewer, Hiroaki Sakai, Adriano M. Alencar, Murilo P. Almeida, José S. Andrade, Arnab Majumdar, Edward P. Inguito, and Béla Suki. Mechanical interactions between collagen and proteoglycans: implications for the stability of lung tissue. *Journal of Applied Physiology*, 98(2):672–679, feb 2005.
- [34] Alexander G Fletcher, Miriam Osterfield, Ruth E Baker, and Stanislav Y Shvartsman. Vertex models of epithelial morphogenesis. *Biophys J*, 106:2291–2304, 2014.

- [35] Silvanus Alt, Poulami Ganguly, and Guillaume Salbreux. Vertex models: from cell mechanics to tissue morphogenesis. *Philosophical Transactions of the Royal Society B: Biological Sciences*, 372:20150520, 2017.
- [36] H.M. Princen and A.D. Kiss. Rheology of foams and highly concentrated emulsions: III. static shear modulus. *J. Colloid Interface Sci.*, 112:427–437, 1986.
- [37] D.A. Reinelt and A.M. Kraynik. Large elastic deformations of three-dimensional foams and highly concentrated emulsions. *J. Colloid Interface Sci.*, 159:460–470, 1993.
- [38] Shuji Ishihara, Philippe Marcq, and Kaoru Sugimura. From cells to tissue: A continuum model of epithelial mechanics. *Physical Review E*, 96:022418, 2017.
- [39] Nebojsa Murisic, Vincent Hakim, Ioannis G Kevrekidis, Stanislav Y Shvartsman, and Basile Audoly. From discrete to continuum models of three-dimensional deformations in epithelial sheets. *Biophys J*, 109:154–163, 2015.
- [40] Satoru Okuda, Yasuhiro Inoue, Mototsugu Eiraku, Taiji Adachi, and Yoshiki Sasaki. Modeling cell apoptosis for simulating three-dimensional multicellular morphogenesis based on a reversible network reconnection framework. *Biomechanics and Modeling in Mechanobiology*, 15:805–816, 2015.
- [41] Sijie Tong, Navreet K. Singh, Rastko Sknepnek, and Andrej Kosmrlj. Linear viscoelastic properties of the vertex model for epithelial tissues. *ArXiv*, page 2102.11181, 2021.
- [42] Sham Tlili, Cyprien Gay, François Graner, Philippe Marcq, François Molino, and Pierre Saramito. Mechanical formalisms for tissue dynamics. *Eur Phys J E Soft Matter*, 38:121, 2015.
- [43] Doron Grossman and Jean-François Joanny. Rheology of 2d vertex model. *ArXiv*, page 2112.04047, 2021.
- [44] Matteo Rauzi, Pascale Verant, Thomas Lecuit, and Pierre-François Lenne. Nature and anisotropy of cortical forces orienting drosophila tissue morphogenesis. *Nat Cell Biol*, pages 1401–1410, 2008.
- [45] Pierre-François Lenne, Jean-François Rupperecht, and Virgile Viasnoff. Cell junction mechanics beyond the bounds of adhesion and tension. *Developmental Cell*, 56:202–212, 2021.
- [46] Soline Chanet, Callie J. Miller, Eeshit Dhaval Vaishnav, Bard Ermentrout, Lance A. Davidson, and Adam C. Martin. Actomyosin meshwork mechanosensing enables tissue shape to orient cell force. *Nature Communications*, 8:ncomms15014, 2017.
- [47] Jonas Ranft, Markus Basan, Jens Elgeti, Jean-François Joanny, Jacques Prost, and Frank Jülicher. Fluidization of tissues by cell division and apoptosis. *Proc Natl Acad Sci U S A*, 107:20863–20868, 2010.

- [48] Steven M Zehnder, Marina K Wiatt, Juan M Uruena, Alison C Dunn, W. Gregory Sawyer, and Thomas E Angelini. Multicellular density fluctuations in epithelial monolayers. *Phys Rev E Stat Nonlin Soft Matter Phys*, 92:032729, 2015.
- [49] Steven M Zehnder, Melanie Suaris, Madison Claire M Bellaire, and Thomas E Angelini. Cell volume fluctuations in mdck monolayers. *Biophys J*, 108:247–250, 2015.
- [50] Liyuan Sui, Silvanus Alt, Martin Weigert, Natalie Dye, Suzanne Eaton, Florian Jug, Eugene W. Myers, Frank Jülicher, Guillaume Salbreux, and Christian Dahmann. Differential lateral and basal tension drive folding of drosophila wing discs through two distinct mechanisms. *Nature Communications*, 9:4620, 2018.
- [51] Hendrik A. Messal, Silvanus Alt, Rute M. M. Ferreira, Christopher Gribben, Victoria Min-Yi Wang, Corina G. Cotoi, Guillaume Salbreux, and Axel Behrens. Tissue curvature and apicobasal mechanical tension imbalance instruct cancer morphogenesis. *Nature*, 566:126–130, 2019.
- [52] Wikipedia. Elastic moduli. https://en.wikipedia.org/wiki/Template:Elastic_moduli, 2022. Accessed: 2022-07-06.
- [53] L.D. Landau, E.M. Lifshitz, A.M. Kosevich, J.B. Sykes, L.P. Pitaevskii, and W.H. Reid. *Theory of Elasticity: Volume 7*. Course of theoretical physics. Elsevier Science, 1986.
- [54] Wikipedia. Bulk modulus. https://en.wikipedia.org/wiki/Bulk_modulus, 2022. Accessed: 2022-07-06.
- [55] Wikipedia. Shear modulus. https://en.wikipedia.org/wiki/Shear_modulus, 2022. Accessed: 2022-07-06.
- [56] Wikipedia. Hooke’s law. https://en.wikipedia.org/wiki/Hooke’s_law, 2022. Accessed: 2022-07-06.
- [57] T A Wilson. A continuum analysis of a two-dimensional mechanical model of the lung parenchyma. *Journal of Applied Physiology*, 33(4):472–478, oct 1972.
- [58] David Boal. *Mechanics of the Cell*. Cambridge University Press, 2012.
- [59] Donald E Ingber, Ning Wang, and Dimitrije Stamenović. Tensegrity, cellular biophysics, and the mechanics of living systems. *Reports on Progress in Physics*, 77(4):046603, apr 2014.
- [60] Ning Wang, Iva Marija Tolić-Nørrelykke, Jianxin Chen, Srboľjub M Mijailovich, James P Butler, Jeffrey J Fredberg, and Dimitrije Stamenović. Cell prestress. i. stiffness and prestress are closely associated in adherent contractile cells. *Am J Physiol Cell Physiol*, 282(3):C606–C616, Mar 2002.

- [61] Jocelyn Étienne, Jonathan Fouchard, Démosthène Mitrossilis, Nathalie Bui, Pauline Durand-Smet, and Atef Asnacios. Cells as liquid motors: Mechanosensitivity emerges from collective dynamics of actomyosin cortex. *Proceedings of the National Academy of Sciences*, 112:2740–2745, 2015.
- [62] Kapil Bambardekar, Raphaël Clément, Olivier Blanc, Claire Chardès, and Pierre-François Lenne. Direct laser manipulation reveals the mechanics of cell contacts in vivo. *Proceedings of the National Academy of Sciences*, 112(5):1416–1421, 2015.
- [63] N.P. Kruyt. On the shear modulus of two-dimensional liquid foams: A theoretical study of the effect of geometrical disorder. *J. Appl. Mech.*, 74:560–567, 2007.
- [64] Jonathan Fouchard, Tom P. J. Wyatt, Amsha Proag, Ana Lisica, Nargess Khalilgharibi, Pierre Recho, Magali Suzanne, Alexandre Kabla, and Guillaume Charras. Curling of epithelial monolayers reveals coupling between active bending and tissue tension. *Proceedings of the National Academy of Sciences*, 117:9377–9383, 2020.
- [65] Tom P. J. Wyatt, Jonathan Fouchard, Ana Lisica, Nargess Khalilgharibi, Buzz Baum, Pierre Recho, Alexandre J. Kabla, and Guillaume T. Charras. Actomyosin controls planarity and folding of epithelia in response to compression. *Nature Materials*, 2019.

Appendix

A. Calculations with GNU-Maxima :

Analytical calculations were performed in the following order with GNU-Maxima :

1. Definition of the variables : geometry and forces
2. Rheological equations
3. Force balance equations
4. Geometry-related equations
5. Calculation of the rest state
6. First-order expansion about the rest state
7. Resolution of the resulting system of equations
8. Monolayer Young modulus
9. Strain along the perpendicular direction and Poisson ratio
10. Expression of other moduli

We include the script used to obtain Eqs. (35-38).

```
kill ( all ) $
/* Definition of variables */
/* geometrical variables about rest state */
assume ( a0 >0);
a : a0 + da$
b : b0 + db$
z : z0 + dz$
p : p0 + dp$
thb : thb0 + dthb$
tha : tha0$
tha0 : %pi /2 $
V : V0 + dV ;
X : 2* b * cos ( thb ) $
X0 : subst ([ db =0 , dthb =0] , X );
Y : a - b * sin ( thb ) $
Y0 : subst ([ da =0 , db =0 , dthb =0] , Y );
eqV : V = X * Y * z$
/* macroscopic deformation variables */
eqEX : EX = (X - X0 )/ X0$
EY : (Y - Y0 )/ Y0$
/* macroscopic stress variables */
Sxx : 1/( X * Y )*(2* suu_a * a * z * cos(tha)^2
+2*2* suu_b * b * z * cos(thb)^2 +2* suu_c * X * Y ) - p * z$
Syy : 1/( X * Y )*(2* suu_a * a * z * sin(tha)^2
+2*2* suu_b * b * z * sin(thb)^2 +2* svv_c * X * Y ) - p * z$
```

```

Szz : 1/ V *(2* svv_a * a * z +2*2* svv_b * b * z ) - p$
/* microscopic deformation variables */
ea : da / a0$
eb : db / b0$
ez : dz / z0$
/* lists of variables for Taylor expansions */
dvec0 : [ da=0, db=0, dz=0 , dV=0 , dp=0, dtha=0, dthb=0, EX=0];
dvec : [ da, db, dz, dV, dp, dthb, EX ];
start : [0, 0, 0, 0, 0, 0, 0];
order : [1, 1, 1, 1, 1, 1, 1];
/* */
/* Rheological equations */
/* microscopic rheological variables */
suu_a : s0l + 2 * gstarl * ea + (kstarl - gstarl) * (ea + ez)$
suu_b : s0l + 2 * gstarl * eb + (kstarl - gstarl) * (eb + ez)$
suu_c : s0h + 2 * gstarh * EX + (kstarh - gstarh) * (EX + EY)$
svv_a : s0l + 2 * gstarl * ez + (kstarl - gstarl) * (ea + ez)$
svv_b : s0l + 2 * gstarl * ez + (kstarl - gstarl) * (eb + ez)$
svv_c : s0h + 2 * gstarh * EY + (kstarh - gstarh) * (EX + EY)$
/* incompressibility */
eqBulk : dV = 0 $
/* */
/* Force balance equations */
/* vertex balance */
eqForces : 2* suu_b * sin ( thb )+ suu_a * sin ( tha )=0 $
/* boundary conditions */
eqSyy : Syy = 0 $
eqSzz : Szz = 0 $
/* */
/* Calculation of the rest state */
eqSyy0 : Syy0 = 0$
eqSzz0 : Szz0 = 0$
eqSxx0 : Sxx0 = 0$
Sxx0 : subst ( dvec0, ev ( Sxx, eval ));
Syy0 : subst ( dvec0, ev ( Syy, eval ));
Szz0 : subst ( dvec0, ev ( Szz, eval ));
eqV0 : subst ( dvec0, ev ( eqV ));
eqForces0 : subst ( dvec0, ev ( eqForces ));
thb0 : rhs ( solve ( eqForces0, thb0 )[1]);
V0 : rhs ( solve ( ev( eqV0 ), V0 )[1]);
p0 : rhs ( factor ( solve ( ev ( eqSzz0, eval ), p0 ))[1]);
z0 : rhs ( solve ( factor ( ev ( eqSxx0, eval )), z0 )[1]);
b0 : rhs ( solve ( factor ( ev ( eqSyy0, eval, eval )), b0 )[1]);
z0 : ev ( z0 );
V0 : ev ( V0, eval );
p0 : ev ( p0 );
/* */
/* First-order expansion about the rest state */
eqForces : factor ( taylor ( ev ( eqForces ), dvec, start, order ));
eqSyy : ev ( eqSyy, eval, eval );
eqSyy : factor ( taylor ( eqSyy, dvec, start, order ));
eqSzz : ev ( eqSzz, eval, eval );
eqSzz : factor ( taylor ( eqSzz, dvec, start, order ));
eqV : factor ( taylor ( ev ( eqV, eval, eval ), dvec, start, order ));

```

```

eqBulk : ev ( eqBulk, eval, eval ) ;
eqBulk : factor ( taylor ( eqBulk, dvec, start, order )) ;
eqEX : factor ( taylor ( ev ( eqEX, eval, eval ), dvec, start, order )) ;
Syst : [ eqForces, eqSyy, eqSzz, eqV, eqBulk, eqEX ] $
/* */
/* Resolution of the resulting system of equations */
[ eqda, eqdb, eqdz, eqdthb, eqdp, eqdV ] :
  solve ( Syst, [ da, db, dz, dthb, dp, dV ])[1] $
da : factor ( rhs ( eqda )) ;
db : factor ( rhs ( eqdb )) ;
dz : factor ( rhs ( eqdz )) ;
dthb : factor ( rhs ( eqdthb )) ;
dp : factor ( rhs ( eqdp )) ;
dV : factor ( rhs ( eqdV )) ;
/* */
/* Monolayer Young modulus */
Sxx : ev ( Sxx, eval ) ;
EstarH3 : factor ( taylor ( Sxx, dvec, start, order ))/ EX ;
/* */
/* Strain along perpendicular direction and Poisson ratio */
Ey : ( factor ( taylor ( EY, dvec, start, order ))) $
Ey : factor ( ev ( Ey )) $
nustarH3 : factor ( - Ey / EX ) ;
/* */
/* Expression of other moduli */
KstarH3 : factor ( EstarH3 /2/(1 - nustarH3 )) ;
GstarH3 : factor ( EstarH3 /2/(1+ nustarH3 )) ;
MstarH3 : factor ( EstarH3 /(1+ nustarH3 )/(1 - nustarH3 )) ;
lambdastarH3 : factor ( MstarH3 * nustarH3 ) ;
/* Non-afinity */
naff : factor((ev(ea)-Ey)/EX) ;
naff : factor(subst(s0h=Psi*s0l,naff));

```

B. The amplitudes of complex moduli does not decrease with frequency

Let us consider a system made of a number of rheological elements arranged in parallel or in series, assuming that each element is either a spring or a dashpot or a fractional element. Fractional elements have moduli of the form $m(\omega) = c_\beta (i\omega)^\beta$, with real prefactors c_β and exponents β between 0 (spring limit) and 1 (dashpot limit). Here, m can be any kind of modulus: shear, compression, etc.

The complex modulus $m(\omega)$ of each element thus has the two following properties: *(i)*, both the real part and the imaginary part of $m(\omega)$ are non-negative, and *(ii)*, the same is true of its derivative $dm/d\omega$ with respect to angular frequency. For a combination in parallel of such elements, moduli add up and so do their derivatives, thus properties *(i)* and *(ii)* are conserved. As a consequence, they also have the property that *(iii)*, the magnitude $|m(\omega)|$ does not decrease with frequency (it is constant in the case of springs).

Combinations in series involve adding up compliances $1/m(\omega)$. These display similar properties, this time with non-negative real parts and *non-positive* imaginary parts, and vice-versa for derivatives. These properties are also conserved under summation. They revert to the initial properties upon inversion and also imply property (iii).

Thus, multiple combinations, in parallel and in series, of elements whose moduli display properties (i) and (ii), such as springs, dashpots and fractional elements, also display these properties.

From the above considerations, we find that the magnitude $|m(\omega)|$ of the complex modulus $m(\omega)$ of the system does not decrease with frequency.

C. 2D hexagonal geometry

In this case, the geometry remains as before, but with $Z = 0$. For clarity, we keep the former 2D notations for cortical tension σ_0 , and where necessary, we use the typical cell height, which we note h_0 and assume constant and equal to $10 \mu\text{m}$.

As in Fig. 2, cell cortices are indexed by a or b depending on their orientations. Cortices along axis y , labeled a , are characterized by a length $\ell_a = \ell_0 + \delta\ell_a$, a 1D tension $h_0 \sigma_a$, equivalent to a 2D stress σ_a and a rheology $\sigma_a = \sigma_0 + \mu \frac{\delta\ell_a}{\ell_0}$ with generalized modulus μ . Similarly, b cortices are characterized by $\ell_b = \ell_0 + \delta\ell_b$, and $\sigma_b = \sigma_0 + \mu \frac{\delta\ell_b}{\ell_0}$, as well by their orientation $\theta = \frac{\pi}{6} + \delta\theta$. Force balance at a vertex now reads $2\sigma_a - 4\sigma_b \sin(\theta) = 0$ where, by symmetry, cortices a remain along direction y upon tissue traction along the x -axis, (see Eq. (16) for comparison). The macroscopic (2D) stress components are expressed as a function of microscopic parameters as:

$$\Sigma_{xx} = \frac{h_0}{S} 4\ell_b \sigma_b \cos^2 \theta - p^{2D}, \quad (81)$$

$$\Sigma_{yy} = \frac{h_0}{S} (2\ell_a \sigma_a + 4\ell_b \sigma_b \sin^2 \theta) - p^{2D}, \quad (82)$$

(see Eqs. (29-30) for comparison).

C.1. Incompressible case

We first consider the intra-cellular material to behave as an inviscid, incompressible fluid, with pressure p^{2D} and constant *area* $S = XY = S_0$.

Our calculation is performed along the same lines as in the 3D case. We find a diverging tissue in-plane bulk modulus K_{2D} (which reflects the assumed incompressibility of each cell within the tissue, $S = S_0$) while the shear modulus reads:

$$G_{2D}(\omega) = \frac{\sigma_0}{\sqrt{3}} \frac{\sigma_0 + 3\mu(\omega)}{\sigma_0 + \mu(\omega)}. \quad (83)$$

The Young and Poisson moduli are obtained according to Eqs. (37-38): since $K_{2D} = \infty$, $E_{2D} = 4G_{2D}$ and $N_{2D} = 1$. In the high-frequency limit $\omega \rightarrow \infty$, where $|\mu(\omega)|$ becomes much larger than σ_0 , expression (83) is bounded and yields $E_{2D}(\infty) = 4\sqrt{3}\sigma_0$, which is

independent of frequency and real, *i.e.*, it corresponds to an elastic rheology, at variance with the power-law behaviour observed experimentally in this limit [14]. In addition, for a realistic value of the cortical tension $\sigma_0 = 0.3$ mN/m [21], we obtain the high frequency limit $E_{2D}(\infty) = 2.1$ mN/m, short of the order of magnitude observed experimentally in suspended monolayers ($E_{2D} \sim 200$ mN/m, corresponding to $E_{3D} = 20 \pm 2$ kPa measured in [12] for $h_0 = 10$ μm).

C.2. Compressible case

In an attempt to circumvent this unsuitable elastic behaviour of our 2D model in the high frequency limit, we questioned the cell incompressibility assumption in the 2D calculation. Indeed, the 3D cell *volume* conservation expected on the time scales relevant to this study is compatible with in-plane variations of the apical cell surface, as the cell height varies correspondingly so as to conserve cell volume. We tested this hypothesis by replacing the incompressibility condition $S = S_0$ by a condition on apical surface variations $dS/S_0 = -dp^{2D}/k_c$ involving the cell pressure p^{2D} and a 2D cell compression modulus k_c . In this case, we find the following expressions of macroscopic moduli which generalize the previous results to finite values of the cell compression modulus k_c :

$$K_{2Dc} = \left(k_c - \frac{\sigma_0}{\sqrt{3}} \right) + \frac{\mu}{\sqrt{3}}, \quad (84)$$

$$G_{2Dc} = \frac{\sigma_0}{\sqrt{3}} \frac{\sigma_0 + 3\mu}{\sigma_0 + \mu}, \quad (85)$$

$$\frac{1}{E_{2Dc}} = \frac{1}{4 K_{2Dc}} + \frac{1}{4 G_{2Dc}}, \quad (86)$$

$$N_{2Dc} = 1 - \frac{2\sigma_0(\sigma_0 + 3\mu)}{\sqrt{3} k_c(\sigma_0 + \mu) + \mu(3\sigma_0 + \mu)}. \quad (87)$$

According to Eq. (86), the high-frequency $\omega \rightarrow \infty$ behaviour of the macroscopic Young's modulus is however unchanged, with an elastic limit $E_{2Dc}(\omega) \rightarrow 4\sqrt{3}\sigma_0$, and remains incompatible with the power-law behaviour observed in this limit. It is easy to show that the complex values of K_{2Dc} and G_{2Dc} belong to the same quadrant of the complex plane. As a consequence, the modulus of $\frac{1}{E_{2Dc}}$ is always larger than the modulus of $\frac{1}{4G_{2Dc}}$. This implies that the modulus of E_{2Dc} is always smaller than its high-frequency limit $E_{2Dc}(\infty) = 4\sqrt{3}\sigma_0$. As was already the case for an incompressible 2D tissue, the order of magnitude of the Young's modulus obtained in the compressible case is incompatible with the experimentally measured value.

C.3. Disordered 2D monolayer

Simulations will be needed to obtain the corresponding results for disordered 2D monolayers, with cells differing for instance in surface area, edge length [63], number of first neighbours or cortex tensions or moduli. Any kind of disorder will in general lead to unequal cell pressures and, correspondingly, to edge curvatures. However, two limiting behaviours can be anticipated.

(i) At low frequencies, since the cortex modulus is negligible as compared to the rest tension σ_0 , the disordered monolayer will behave elastically at small deformations. Its moduli will be proportional to σ_0 (just like in the ordered case) as results from dimensional analysis, a fact that is well known in the liquid foam community [29, 30].

(ii) By contrast, in the large frequency limit, unless the cortex rheology is purely elastic in that limit, the cortex modulus will dominate over the rest tension ($|\mu|/\sigma_0 \rightarrow \infty$). Thus, unless all cortices remain undeformed at first order, the corresponding forces proportional to μ will become dominant within the macroscopic stress. Now, as for cortex deformation, it is to be expected that, for general disordered networks as opposed to the ordered, honeycomb structure, there will exist no deformation mode that will conserve both each cell cytoplasm surface area *and* each edge length, at first order. As a result, any macroscopic deformation will result in at least some cell-cell junctions changing their lengths. The corresponding tensions, and hence the macroscopic stress, will therefore be sensitive to the cell cortex rheological modulus, μ .

D. Affine behaviour

As mentioned in Section 2.2, some elements in the cell deform in a non-affine manner, that is, not in the same proportions as the monolayer.

In order to demonstrate that, let us consider how two quantities are affected by the applied deformation ϵ_x , namely: (i) the deformation $\epsilon_a = \ell_a/\ell_0$ of the a facets, defined by Eq. (22), and (ii) the transverse deformation ϵ_y of the representative volume, defined by Eq. (19). Of course, because we are considering linear response, they are both proportional to the applied deformation ϵ_x . For the sake of clarity, let us assume that the monolayer is being stretched in the x -direction ($\epsilon_x > 0$). As a result, it shrinks in the y -direction ($\epsilon_y < 0$). As for the a facets, three options are possible, as shown on Fig. 6. The a facets can shrink exactly like the sample (affine deformation $\epsilon_a = \epsilon_y < 0$, Fig. 6b). They can shrink more than the sample ($\epsilon_a < \epsilon_y < 0$, Fig. 6c). They can shrink less ($\epsilon_y < \epsilon_a \leq 0$, Fig. 6d).

Hence, it appears reasonable to evaluate the difference between ϵ_a and ϵ_y , divided by the applied deformation, and choose it as an *indicator of non-affinity* for the monolayer subjected to the present deformation, which we name \mathcal{N} :

$$\mathcal{N} \equiv \frac{\epsilon_a - \epsilon_y}{\epsilon_x} \quad (88)$$

$$= \frac{(k_L + g_L - \sigma_{0L})(2k_H + \Psi(3\sigma_{0L} + k_L + 9g_L))}{\mathcal{D}}, \quad (89)$$

$$\begin{aligned} \mathcal{D} = & 4\Psi\sigma_{0L}^2 + 2(k_H + g_H)\sigma_{0L} + (7k_L + 15g_L)\Psi\sigma_{0L}, \\ & + 2(k_H + g_H)(k_L + g_L) + \Psi(k_L^2 + 10g_L k_L + 9g_L^2). \end{aligned} \quad (90)$$

The non-affinity indicator \mathcal{N} turns out to be nonzero unless a very specific condition is met:

$$k_L + g_L = \sigma_{0L}. \quad (91)$$

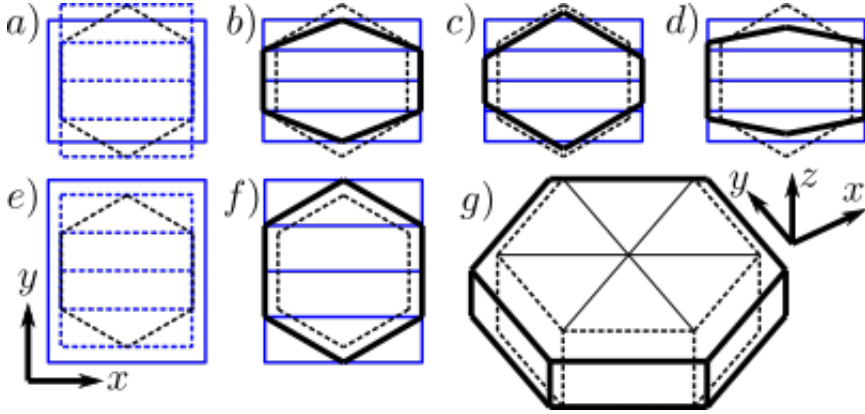


Figure 6.: **Deformation modes.** (a-d): the monolayer is stretched in the x -direction. (e-g): the monolayer is stretched isotropically in the x - y plane. (a, e): the blue dashed rectangle with intermediate lines is a guide for the eye that matches the undeformed (dashed) hexagon. The corresponding rectangle after deformation is drawn with a blue, solid line. (b, f): the deformation is affine (hexagon deformation matches overall deformation, see intermediate blue lines, which implies $\epsilon_a = \epsilon_y$), when (b) $\mathcal{N} = 0$ or when (f) the deformation is isotropic. (c): a facets shrink more ($\epsilon_a < \epsilon_y < 0$, $\mathcal{N} < 0$) than the overall sample (compare deformed hexagon and intermediate blue lines). (d): a facets shrink less ($\epsilon_y < \epsilon_a \leq 0$, $\mathcal{N} > 0$) than the overall sample (compare deformed hexagon and intermediate blue lines). (g): under isotropic in-plane stretching, while horizontal facets are stretched isotropically, lateral facets are elongated along their respective horizontal directions in the x - y plane and shrink along direction z .

This expression can be partly understood qualitatively. In the limit where the facet moduli k_L and g_L are much smaller than the rest tension σ_{0L} (this corresponds to the low frequency limit), the tensions will remain unchanged by the deformation, and it is expected that the angles between lateral facets, which result from the force balance, remain equal to their initial value, $2\pi/3$ (see Fig. 6c). It is obvious that the a facets then shrink more than the overall sample (see blue lines for comparison). And indeed, \mathcal{N} is then negative, consistently with the fact that $k_L, g_L \ll \sigma_{0L}$. By contrast, when k_L and g_L are much larger than σ_{0L} (this corresponds to the high frequency limit), the facets are purely elastic and their dimensions tend to keep constant dimensions (see Fig. 6d). It is obvious that the a facets then shrink less than the overall sample, and indeed, \mathcal{N} is positive in this limit.

Let us recall that the calculation in the present work was carried out using the simplifying assumption, stated in Section 2.2, that basal and apical facets deform affinely, *i.e.*, according to the overall deformation, measured by ϵ_x and ϵ_y . That assumption is expressed through Eq. (20) for the stress in those facets (assumed uniform), as well as through Eq. (16) which states that the vertical edge where lateral facets meet receives

no forces from the horizontal facets.

Whenever ϵ_a and ϵ_y differ according to the present calculation, the edges where lateral facets meet (hexagon corners) and the initially corresponding points of the horizontal facets *do not coincide* after the overall deformation has been applied (see mismatch between the hexagon corners and the intersections of blue lines in Figs. 6c-d). Yet such a point is in reality the corner of three neighbouring cells, and obviously the horizontal facets should remain attached to the lateral facets! Thus, in reality these corresponding points are maintained attached to each other (through a tensile force) and the real deformation of facets a adopts some intermediate value between ϵ_y and the value of ϵ_a calculated here. In other words, the sign of \mathcal{N} is correct, but its magnitude is somewhat overestimated in the framework of the present assumption.

Note that unless the cortex rheology is purely elastic in some frequency range (*i.e.*, with real moduli), there is no frequency where condition (91) can be satisfied, hence the deformation is always somewhat non-affine.

For the sake of completeness, let us mention that we have also explored several refined geometrical descriptions of the horizontal facet kinematics. Although they did fix the mismatch between lateral facet vertical edges and horizontal facets, none of them was both reasonably simple and six-fold symmetric. Hence, we resolved to keep the present version, albeit somewhat inconsistent as detailed in the present Appendix. Only with a highly refined mesh both in the horizontal and the lateral facets can one hope to fully deal with this issue and calculate the exact amplitude of the non-affine deformations in the monolayer. That is beyond the scope of the present work.